Journal of Environmental Chemical Engineering 11 (2023) 110525

Contents lists available at ScienceDirect

Journal of Environmental Chemical Engineering

journal homepage: www.elsevier.com/locate/jece

# Integrated photoelectrochemical (PEC)-forward osmosis (FO) system for hydrogen production and fertigation application

Sifani Zavahir [a], Tasneem Elmakki [a,b], Mona Gulied [a], Ho Kyong Shon [c], Hyunwoong Park [d], Konstantinos E. Kakosimos [e], Dong Suk Han [a,b,f,*]

[a] Center for Advanced Materials, Qatar University, PO Box 2713, Doha, Qatar
[b] Materials Science and Technology Master Program, College of Arts and Science, Qatar University, PO Box 2713, Doha, Qatar
[c] Center for Technology in Water and Wastewater, School of Civil and Environmental Engineering, University of Technology Sydney, Sydney, NSW 2007, Australia
[d] School of Energy Engineering, Kyungpook National University, Daegu 41566, the Republic of Korea
[e] Chemical Engineering Program, Texas A&M University at Qatar, Doha, Qatar
[f] Department of Chemical Engineering, Qatar University, PO Box 2713, Doha, Qatar

ARTICLE INFO

Editor: Xin Yang

*Keywords:*
Forward osmosis (FO)
Photoelectrochemical (PEC) system
Water-energy-food nexus
Hydrogen
Fertigation

ABSTRACT

This study proposes an integrated system that combines a photoelectrochemical (PEC) system and forward osmosis (FO) system in tandem operation to address water, energy, and food (WEF) scarcity. The system utilizes a combination of ammonium sulfite and ammonium sulfate solution to represent wet flue gas desulfurization products from the ammonia scrubbing process commonly used in oil and gas producing countries. Under simulated sunlight, the sulfurous solution in the PEC system is oxidized at a reduced titania nanotube array (TNA) working electrode to produce hydrogen, a clean energy source (Energy). The oxidized sulfurous solution entering the draw solution (DS) compartment of the FO unit was then diluted when the FO system operates against simulated brackish water as the feed solution (FS, Water). The DS effluent is recirculated to ensure continuous operation of both PEC and FO systems. At a certain point in time, the DS effluent is also used as a cultivation solution for basil plants, the growth is visually more favorable compared to those supplied with tap water (Food). A concentrated DS (0.8:0.2 ratio of $(NH_4)_2SO_3$:$(NH_4)_2SO_4$) showed excellent water desalination performance. It had a high water flux of 17 LMH with 11.8 % water recovery, highest salt rejection (98.6 % for $Na^+$ and 98.3 for $Cl^-$), and lowest reverse solute flux (RSF) (3.5 $g{\cdot}m^{-2}{\cdot}h^{-1}$ for $SO_4^{2-}$, 5.25 $g{\cdot}m^{-2}{\cdot}h^{-1}$ for $SO_3^{2-}$, 3.1 $g{\cdot}m^{-2}{\cdot}h^{-1}$ for $NH_4^+$) against 5 $g{\cdot}L^{-1}$ NaCl FS for 5 h, with a cathodic current density of 0.15 $A{\cdot}cm^{-2}$. Overall, this study demonstrates the successful implementation of a bench-scale integrated system that produces tangible outcomes for water, energy, and food.

## 1. Introduction

Until the 1950s, basic human needs were limited to food, water, shelter, and clothing. However, the rise of automated mass production of electronics and computers has made energy an additional essential need. Governments now strive to ensure sufficient electrical power for domestic use, despite high consumption in industrial facilities. Fossil fuels-burning power plants, such as coal and fuel, emit harmful flue gases containing SOx, carbon, and NOx [1]. The SOx concentration in flue gas depends on coal's sulfur content. For instance, a pulverized coal-fired power plant using 2.8 % sulfur coal releases 2000 ppm of $SO_2$ in the exhaust gas [2]. Sulfur gas concentrations in steam boiler fumes can range from 4.4 to 2 $mg{\cdot}mol{\cdot}L^{-1}$, depending on fuel throughput [3].

Strict air quality standards have been implemented by governments to protect the environment, including the oceans, from these emissions. High atmospheric sulfur levels can cause acid rain and affect aquatic life. Consequently, sulfur removal from flue gases has become a critical research area, with flue gas desulfurization (FGD) emerging as a prominent field employing regenerative and non-regenerative scrubbers to absorb and remove $SO_2$ [4]. FGD with ammonia is a relatively new technique in which $SO_2$ is absorbed in aqueous ammonia ($NH_3$) to form $(NH_4)_2SO_3$ or $(NH_4)_2SO_4$, as depicted in reactions R1-R2. This method is preferred over other techniques due to the low parasitic load experienced in ammonia scrubbing [5].

* Corresponding author at: Center for Advanced Materials, Qatar University, PO Box 2713, Doha, Qatar.
*E-mail address:* dhan@qu.edu.qa (D.S. Han).

https://doi.org/10.1016/j.jece.2023.110525
Received 27 January 2023; Received in revised form 17 May 2023; Accepted 5 July 2023
Available online 7 July 2023

.

Ensuring self-sufficiency in water, energy, and food (WEF) is vital for a secure society. In recent years, there has been a growing awareness of the interconnection between these essential resources, leading to increased research and policy discussions to develop strategic planning and holistic frameworks for WEF security [6–11]. Numerous nexus studies examine strategies and improved frameworks for WEF security in various countries or regions [12–14]. The expanding population and material consumption intensify the pressure on the WEF nexus, emphasizing the need for solutions [11]. Veroneau et al. demonstrated continuous operation of an electrochemical (EC) system and sustainable generation of oxygen- and hydrogen-based energy through water splitting using seawater concentrated with forward osmosis (FO) [15]. Logan et al. highlighted the importance of producing hydrogen using renewable energy sources and seawater electrolysis [16].

In line with this, this study aims to develop a self-sustainable combined system utilizing treated environmental pollutants ($(NH_4)_2SO_3$ and $(NH_4)_2SO_4$, produced in the FGD ammonia scrubbing process) as initial feed resources to produce WEF with minimal energy consumption. The research was conducted in Qatar, a country whose economy is heavily dependent on natural gas extraction and refining, resulting in the release of sulfur-containing flue gasses into the atmosphere [17]. Our previous work demonstrated the effective use of ammonium sulfite and ammonium sulfate as a draw solution (DS) in a fertilizer-drawn forward osmosis (FDFO) system [18]. In the salinity gradient-driven FO system, a high concentration of sulfur-based seed solution (SBSS) was employed as a fertilizer DS, which is then diluted by recovering water from brackish level water serving as the feed solution (FS). Our findings revealed that a lower sulfite content in the DS led to enhanced desalination performance.

To address WEF needs, we further modified the FO system using brackish water as FS and SBSS derived from FGD as DS. The FDFO system requires neither high pressure for desalination, like RO, nor energy to recover draw solutes from mixed DS, as in typical FO system [19–21]. The electron donor ability of SBSS can be harnessed for hydrogen evolution through EC water splitting. Using a suitable light-harvesting electrode, the EC system can be converted into a photoelectrochemical (PEC) system, making it more environmentally friendly [22,23]. Additionally, the diluted DS, rich in N and S, can be used as a fertilizer in fertigation.

This study successfully demonstrates the synchronized operation of a bench-scale PEC-FDFO integrated system, monitoring performance in terms of DS dilution level, salt rejection, and water recovery rate (Water), as well as stability and photocurrent level of hydrogen evolution (Energy). Basil plants growth (Food) fed with diluted DS was assessed through visual observation and periodic photographs, showcasing the FGD products' utilization for achieving net-zero sulfur emissions.

## 2. Materials and methods

### 2.1. Chemicals

The chemicals used for electrode fabrication included phosphoric acid ($H_3PO_4$, 85 %, Sigma-Aldrich, China), sodium fluoride (NaF, 99 %, Sigma-Aldrich, China), ethylene glycol ($(CH_2OH)_2$, 99.5 %, Scharlab, Spain), ethanol ($C_2H_5OH$, 99.7 %, Scharlab, Spain), and acetone ($(CH_3)_2CO$, 99.8 %, Emsure, Germany). The PEC electrolyte, DS, and FS were prepared using ammonium sulfite solution ($(NH_4)_2SO_3$, 35 % in $H_2O$, Sigma-Aldrich, India), ammonium sulfate ($(NH_4)_2SO_4$, 98.5 %, Sigma-Aldrich, India), and sodium chloride (NaCl, 99.5 %, VWR chemicals, Belgium). All chemicals were of analytical grade and used without further purification. Both the model FS and DS were prepared by dissolving specific amounts of chemicals in deionized water (DIW). DIW was obtained from a Milli-Q water purification system (Fischer Scientific, Waltham, MA, USA) with a resistivity of 18.2 MΩ at 25 °C.

### 2.2. Experimental setup of FDFO-PEC system

Fig. 1b and c show the bench-scale setup of the integrated system used in this study, consisting of two interconnected subsystems: a PEC system generating hydrogen gas using a sulfur-based seed solution (SBSS) as an electrolyte and a forward osmosis (FO) system utilizing the circulated SBSS from the PEC system as the DS against brackish level simulated NaCl solution as FS (i.e., concentration of 3 $g{\cdot}L^{-1}$ (3.25 $mS{\cdot}cm^{-1}$, 1.26 bar) for 0.24 M SBSS and 5 $g{\cdot}L^{-1}$ (5.80 $mS{\cdot}cm^{-1}$, 2.11 bar) for 1 M SBSS). The initial FO operation circulates 3 L of FS and 1 L of DS.

The PEC system features a customized two-compartment cell (12 × 12 cm) with a three-electrode system configuration, including a fabricated titania nanotube (TNA) electrode (working electrode), Pt wire, and saturated calomel electrode (SCE) as the counter and reference electrodes, respectively. A spacer and Nafion membrane (0.16 mm thick) separate the compartments, facilitating proton transfer during the experiment. Electrochemical data acquisition and analysis were performed using a potentiostat/galvanostat (Gamry, interface™ 1010, USA). A SunLight™ solar simulator (ABET Tech., Inc., USA) provided one sun intensity (AM 1.5 G, 100 $mW{\cdot}cm^{-2}$) to drive photon-based electrochemical reactions.

The FDFO system comprises a handmade FO test cell, two variable gear pumps (Model 75211-15, Cole-Parmer, USA), two flow meters (Model 132461-42, Cole-Parmer, USA), and FS and DS tanks. The FO cell has a symmetric channel on either side of the membrane, with water circulating in a closed loop from the FS side to the DS side. Instantaneous DS weight changes were recorded using a digital scale balance connected to data logger software. A commercial flat sheet thin-film composite (TFC) membrane provided by Toray Industries, Inc., Japan, with an effective surface area of 36 $cm^2$, was used for FDFO tests. The membrane characteristics included a water permeability coefficient (A) of 2.07 $L{\cdot}m^{-2}{\cdot}h^{-1}{\cdot}bar^{-1}$, salt permeability coefficient (B) of 0.49 $kg{\cdot}m^{-2}{\cdot}h^{-1}$, and structural parameter (S) of 204 μm.

All tubes and fittings were 3/8″ and 6″ sizes, respectively. A peristaltic pump (Cole Palmer, Masterflex L/S) facilitated the passage of the SBSS solution from the PEC cell's outlet to the inlet on the DS side of the FO cell.

### 2.3. Electrode fabrication, characterization, and testing

A modified anodization technique was employed to fabricate highly

$$SO_2(g) + NH_3(g) + H_2O \xrightarrow{\text{chemical absorption}} (NH_4)_2SO_3(aq) \quad (R1)$$

$$(NH_4)_2SO_3(aq) + O_2 \xrightarrow{\text{air oxidation}} (NH_4)_2SO_4(aq) \quad (R2)$$

$$(NH_4)_2SO_3(aq) + H_2O \xrightarrow{\text{electrolysis}} (NH_4)_2SO_4(aq) + H_2 \quad (R3)$$

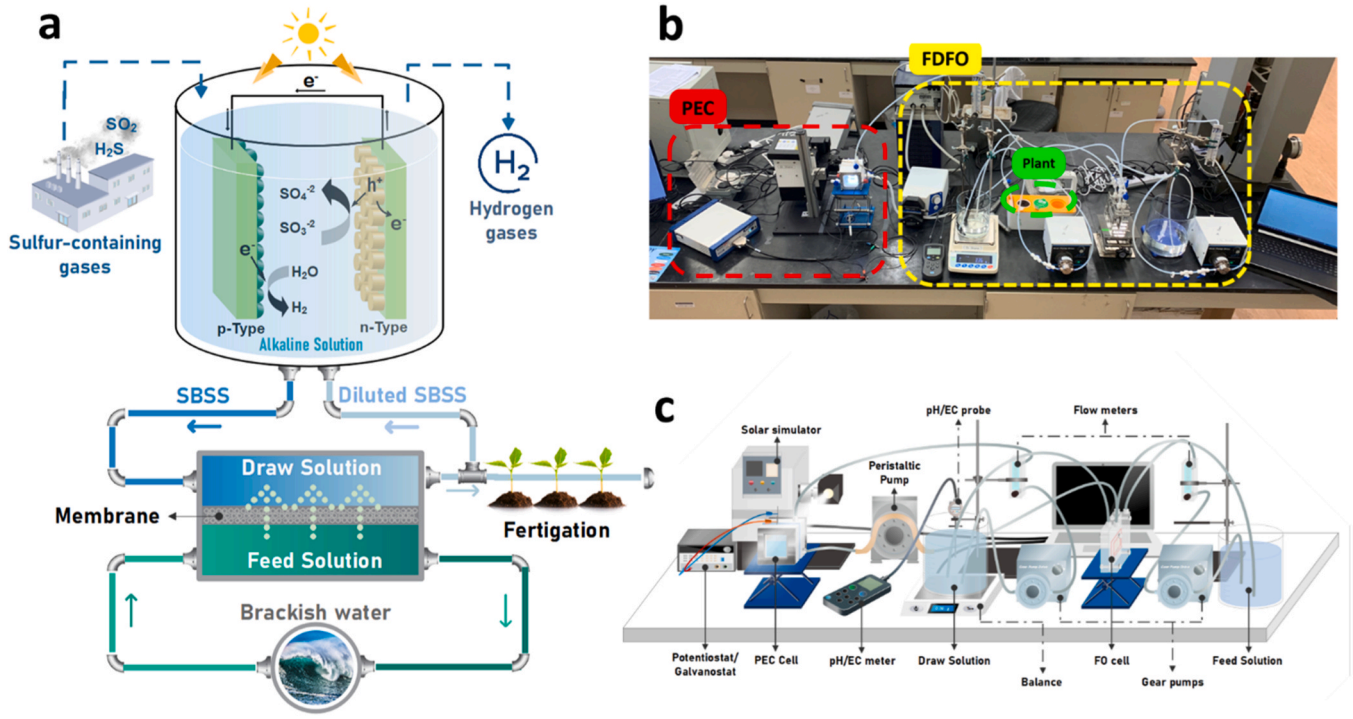


**Fig. 1.** From concept to experimental setup of an integrated water-energy-food (WEF) system. (a) Schematic representation of the solution for the water-energy-food nexus modeled in this study. (b) Photograph of a bench-scale PEC-FDFO setup. (c) Schematic diagram of a bench-scale PEC-FDFO hybrid system with performance evaluation devices such as salinity, pH meters, and scales.

ordered titania nanotube electrodes. Titanium (Ti) sheets (2 cm × 4 cm, 0.127-mm thick, 99.7 % purity, Sigma-Aldrich) were cut, polished using sandpaper (400 grid) and a polishing cloth, and then cleaned for 10-min in an ultrasonication bath (40 kHz, 100 W power, WiseClean, Germany) with acetone and ethanol, followed by nitrogen gas drying. The Ti electrodes were electrochemically anodized against a stainless-steel plate (3 cm × 5 cm) by applying a DC current of + 30 V and 0.04 A for 4 h in a solution containing dissolved $H_3PO_4$ (0.55 M) and NaF (0.14 M) in an aqueous electrolyte solution with a 4:1 ratio of DIW to ethylene glycol. The solution was continuously stirred throughout the anodization. The as-obtained anodized electrodes were then thoroughly washed with DIW and ethanol and dried in ambient air. The anodized TNA electrodes were annealed at 400 °C (annealed TNA) for 2 h and electrochemically reduced to black $TiO_2$ (reduced TNA) by applying a counter-current of - 40 V against a Pt counter electrode in a phosphate buffer medium (0.1 M $KH_2PO_4$ buffer solution, pH 7.2) for 6 min

The fabricated electrode material, active layer (AL), and support layer (SL) of the FDFO membrane were characterized using scanning electron microscopy equipped with energy dispersive X-ray spectroscopy (SEM/EDX, NOVANANOSEM 450, USA). X-ray diffraction (XRD, PANalytical Empyrean, UK) confirmed the crystallographic structures of TNA electrodes at various fabrication steps in the $2\theta$ angle range from 20° to 70°. Surface roughness and depth were measured using a profilometer (Leica DMC 8 Profilometer, Germany). Functional groups of the AL and SL were analyzed using Fourier transform infrared (FTIR-ATR, Spectrum 400 Perkin Elmer, USA) in the region of 4000–550 $cm^{-1}$ with a scan rate of 32 scans. The surface energy of the FDFO membrane was calculated using the Owens, Wendt, Rabel, and Kaelble (OWRK) model, which involved measuring the optical contact angles of water, ethylene glycol, and formamide on the membrane. Contact angle measurements were conducted using an OCA 35 device (DataPhysics, Germany), with a solvent volume of 3 μL dispensed, and images captured after 5 s. Five measurements were taken for each solvent at different locations on the cut membrane. To assess the thermal stability of the membrane material, thermogravimetric analysis (TGA) was performed from room temperature (RT) to 450 °C using a TGA400 instrument (Perkin Elmer, USA) under a nitrogen atmosphere with a gas flow rate of 90 mL·$min^{-1}$.

The electrochemical properties of the fabricated electrodes were characterized using cyclic voltammetry (CV), chronoamperometry, and electrochemical impedance spectroscopy (EIS) tests. CV tests evaluated the hydrogen evolution reaction (HER) on the electrode within a + 1.2 V to − 1.2 V vs. SCE at a scan rate of 50 mV·$s^{-1}$. During light-on experiments, the solar simulator, calibrated to 1 sun illumination intensity (100 mW·$cm^{-2}$), was directed to the working electrode, while it was turned off for the dark experiments. Photoactivity and stability were assessed by performing chopped chronoamperometry at − 0.25 V vs. SCE and EIS tests to evaluate the ohmic resistance in a 100 kHz to 0.01 Hz frequency range. The solar simulator's inbuilt light shield enabled intermittent light chopping. Electrochemical performance tests utilized single or binary electrolyte solutions based on ammonium sulfate or/and ammonium sulfite, with initial solution concentrations provided in Table 1.

### 2.4. Evaluation of FDFO-PEC system

The integrated system experiments started with the PEC side, initially stabilizing the PEC cell by introducing DIW as the electrolyte solution. A chronoamperometric test was conducted at − 1.0 V for 3 min, followed by another similar test with the DS. Subsequently, the PEC and FDFO systems were operated simultaneously. The PEC cell was filled with the test electrolyte solution, and a chronoamperometry scan was performed for 5 h at − 1.0 V with a scan rate of 50 mV·$s^{-1}$. In each experiment, DS flowed into the DS tank, passed through the PEC cell, and entered the FO cell's inlet.

On the FDFO side, all tests were conducted in FO mode, with the AL of the FO membrane facing the FS and the support layer facing the DS. The FDFO system was initially stabilized using DIW as FS and DS for 30 min. Several FDFO tests were performed by varying the flow rates of FS and DS solutions (0.5, 0.8, and 1.0 L·$min^{-1}$ (LPM)) and the operating time (6 and 24 h). During these tests, the temperature of FS and DS was

**Table 1**
Properties of SBSS based DS concentrations at temperature of 25 °C ± 1 and pressure of 1 bar.

| DS | Molar concentration (M) | | Conductivity (mS·cm$^{-1}$) | Osmotic pressure (bar)[a] |
|---|---|---|---|---|
| | $(NH_4)_2SO_4$ | $(NH_4)_2SO_3$ | | |
| DS1 | 0.24 | | 28.0 | 6.26 |
| DS2 | 0.144 | 0.096 | 24.6 | 6.20 |
| DS3 | 0.12 | 0.12 | 24.4 | 6.19 |
| DS4 | 0.096 | 0.144 | 22.7 | 6.17 |
| DS5 | | 0.24 | 23.4 | 6.12 |
| DS6 | 1 | | 99.3 | 31.12 |
| DS7 | | 1 | 92.6 | 28.03 |
| DS8 | 0.8 | 0.2 | 96.1 | 30.43 |
| DS9 | 0.6 | 0.4 | 97.5 | 29.78 |
| DS10 | 0.4 | 0.6 | 93.6 | 29.16 |
| DS10 | 0.2 | 0.8 | 91.9 | 28.58 |
| DS11[b] | 0.1 | 0.4 | 54.5 | 13.67 |

[a] Osmotic pressure estimated from AspenPlus software (Aspen ONE® version 9 software Aspen Technology. Inc., using nonrandom two-liquid (NRTL) model in 'Aspen Physical Property System Data Regression System').
[b] DS concentration is 0.5 M, prepared to be half the molarity of DS 10.

maintained at room temperature (25 °C ± 1) without mixing. In-situ hydraulic flushing or forward cleaning was applied after each FDFO run using DIW as FS (1 L) and DS (1 L) at a fixed circulation flow (1 LPM), cross flow velocity (0.28 m·min$^{-1}$) on both sides of the FO test cell, and at room temperature (25 °C ± 1) for 30 min to reduce membrane fouling. The water quality of FS and DS was analyzed before and after each run using a benchtop conductivity and pH meter (HQ portable meter, HACH, USA) and ion chromatography (850 Professional Metrohm, Switzerland). The performance of the FDFO process was evaluated in terms of water flux ($J_w$, L·m$^{-2}$·h$^{-1}$), reverse solute flux (RSF, $J_s$, g·m$^{-2}$·h$^{-1}$), and salt rejection percentage (R %). The experimental water flux was calculated by dividing the weight changes of DS ($\Delta W$, kg) over the operating time ($\Delta t$, h) and effective membrane area ($A_{eff}$, m$^2$), as expressed in Eq. (1).

$$J_w = \frac{\Delta W}{(\rho A_{eff} \Delta t)} \tag{1}$$

The reverse solute flux of each individual component in DS ($NH_4^+$, $SO_4^{2-}$, and $SO_3^{2-}$) can be determined using Eq. (2):

$$J_s = \frac{(V_i - V_P)C_r}{A_{eff} \quad t} \tag{2}$$

where $V_i$ and $V_p$ represent the initial volumes (in L) of FS and the permeate volume of pure water from FS to DS, respectively. $C_r$ (g·L$^{-1}$) is the concentration of draw solutes in the feed side at the end of the experiment, and t is the experiment's operating time.

The salt rejection percentage (R %) of ions in FS ($Na^+$, $Cl^-$) that may diffuse through the FO membrane from the feed side to the draw side is expressed in Eq. (3).

$$R\% = \frac{C_{F_i} - \frac{C_{D_f}(V_i - V_P)}{V_P}}{C_{F_i}} \tag{3}$$

where $C_{F_i}$ and $C_{D_f}$ are the initial and final concentrations of ions in FS and DS, respectively.

### 2.5. Draw (DS) and feed solution (FS) preparation

Ammonium sulfate ($(NH_4)_2SO_4$) and ammonium sulfite ($(NH_4)_2SO_3$) were used as DS. Two different concentration categories were studied: diluted and high concentrations. For diluted concentrations, FS contained 3 g·L$^{-1}$ NaCl, while DS ranged from 0.16 M to 0.36 M $(NH_4)_2SO_4$ solution as the single-component DS. Binary mixtures of $(NH_4)_2SO_4$ and $(NH_4)_2SO_3$ with a total salt concentration of 0.24 M were coupled with 3 g·L$^{-1}$ NaCl FS prior to using high concentrations of DS in the upscaled PEC-FDFO system. For high concentrations, FS had 5 g·L$^{-1}$ NaCl, and DS contained a total salt concentration of 1 M prepared with $(NH_4)_2SO_4$ or $(NH_4)_2SO_3$ in DIW. Detailed characteristics of 1 M DS are given in Table 1.

### 2.6. Evaluation of basil plant growth

The impact of diluted DS on plant growth was assessed by comparing two basil plants grown side by side, one fed with municipal water and the other with diluted DS. Each plant received 25 mL of water daily and was exposed to sunlight. Municipal water quality data can be found in Table S1. Plant growth was monitored through periodic photographs, leaf count, and measurement of stem and branch height.

## 3. Results

### 3.1. Characterization of TNA electrode

During PEC operation, a sulfur-based seed solution (SBSS) prepared with ammonium sulfate and/or ammonium sulfite in aqueous media is introduced into the PEC cell. SBSS acts as the catholyte electrolyte and produces hydrogen gas via water electrolysis in the PEC system with reduced titania nanotube arrays cathode upon solar light illumination. The morphology of the reduced TNA is a high-order tubular array, confirmed by FE-SEM in Fig. 2a. TNAs grown on Ti film by anodization technique offer two advantages: facilitating commercial-scale applications [24,25] and providing better stability and adhesion between the electroactive film and the substrate [26,27]. A well-defined, hollow--centered arrays in the reduced TNA is retained throughout the annealing and reduction process (Fig. S1). XRD analysis reveals sharp peaks at 25.30°, 38.57°, and 48.02°, corresponding to the presence of (101), (004), and (200) planes, confirming the anatase phase crystallization during annealing (Fig. 2b). Similar observations were made by Jeong et al. when fabricating TNA in an anodization mixture with 2 % of DIW in ethylene glycol electrolyte [26]. XRD shows anatase phase formation during annealing and its presence throughout the reduction process. The anatase phase titania is widely studied for various UV light-utilizing applications [28,29].

Creating oxygen vacancies by reducing some $Ti^{4+}$ sites in titania shifts the band edge slightly towards the visible region. The photoluminescence (PL) spectra recorded for the annealed and reduced electrodes upon 375 nm excitation showed higher PL intensity for the annealed electrode, which decreased significantly for the reduced electrode (Fig. 2c). As PL intensity is related to electron-hole recombination rate, the reduced TNA exhibits a lower charge recombination rate, facilitating higher light-induced activity. In addition, the band structure calculated from the PL spectra reveals a bandgap of 2.75 eV for the reduced TNA. Surface topography analysis shows a relatively smooth surface on the reduced TNA electrode with a surface roughness parameter of 0.5536 μm (Fig. 2d), which increased to 0.6376 μm when annealed (Fig. S2), indirectly confirming the reduction process's success.

### 3.2. Photoelectrochemical (PEC) performance

In the integrated system, the reduced TNA functions as the PEC cathode electrode. Its light-induced electrochemical behavior was evaluated in a standalone process operation using a singular $(NH_4)_2SO_4$ electrolyte and compared to anodized and annealed counterparts. CV tests conducted in a 0.1 M $(NH_4)_2SO_4$ electrolyte solution demonstrated the TNA electrodes' capability for hydrogen gas production upon light illumination (Fig. 3a). The onset potential, a crucial parameter for evaluating hydrogen production efficiency, showed a favorable trend with reduced TNA electrodes at − 0.06 V, compared to anodized and annealed electrodes at − 0.36 V, − 0.12 V, respectively (Fig. 3a). This

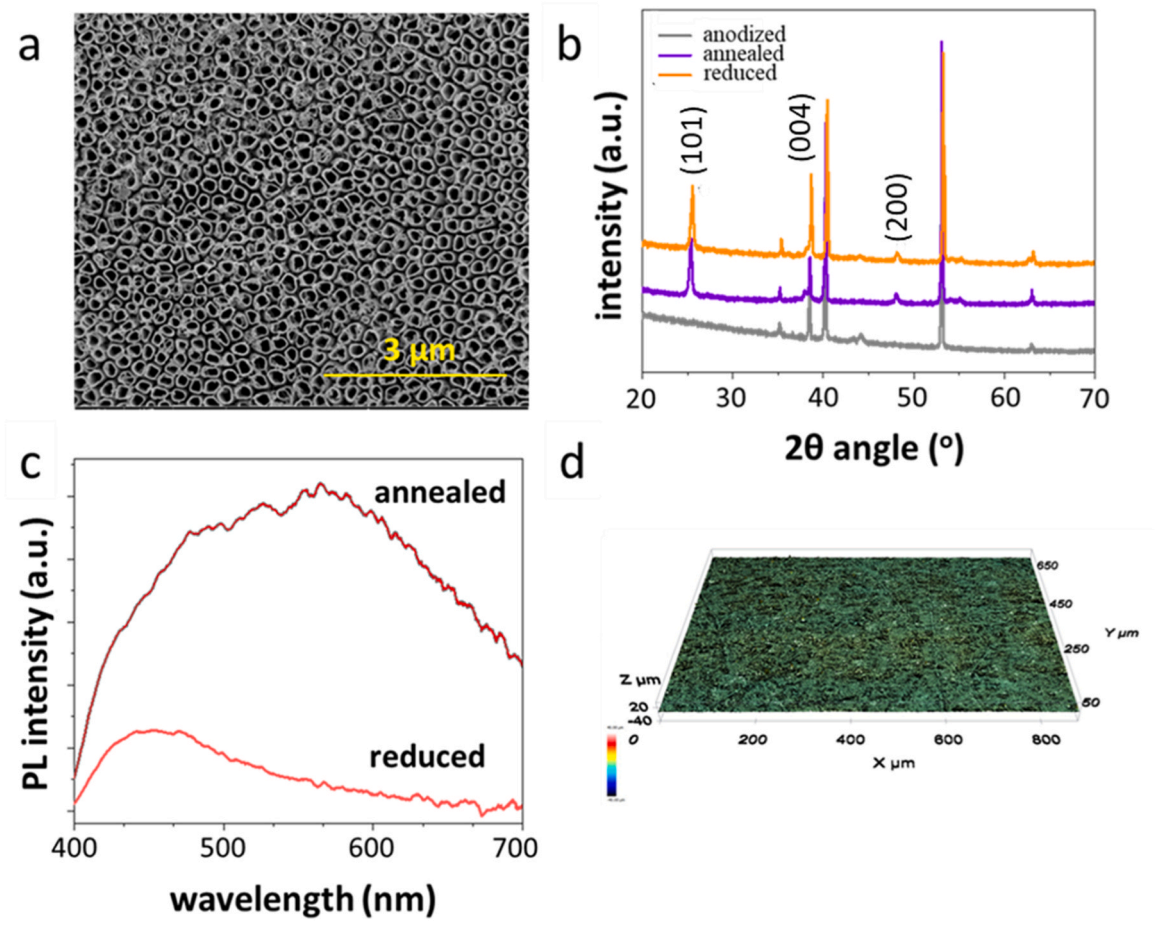


**Fig. 2.** Surface analysis of titania nanotube array (TNA) electrodes. (a) SEM image of a reduced TNA electrode. (b) XRD data collected in the 2$\theta$ angle range from 20° to 70° (anatase diffraction angles indexed). (c) PL intensity in the 400–700 nm range upon excitation at 375 nm. (d) Surface topography of a reduced TNA electrode captured by a profilometer.

indicates a favorable trend towards improved hydrogen production efficiency with the reduced TNA electrode. The reduced TNA electrode exhibited a high current density of $-7$ mA·cm$^{-2}$ at $-0.6$ V (vs. SCE), significantly higher than the maximum current density of $-0.1$ mA·cm$^{-2}$ observed in a previous study using 0.1 M $Na_2SO_4$ electrolyte and TNA material on FTO glass [26]. In the present study, the scan rate was maintained at 50 mV·s$^{-1}$, higher than the 5 mV·s$^{-1}$ used in the previous study. The scan rate can affect the limited diffusion current in cases where a reaction is diffusion-controlled, leading to higher current densities at increased scan rates.

The stability and progression of electrochemical reactions were evaluated using chronoamperometry. The chopped chronoamperometric test, typically performed on PEC systems, provided additional information on photo-induced chemical reactions by producing crest and trough for light on and off regions, respectively (Fig. 3**b**). This test, conducted at $-0.25$ V (vs. SCE), displayed a significant increase in light-induced photoactivity of the reduced TNA compared to annealed TNA electrode, while the anodized electrode showed no activity, as expected due to its higher onset potential (−0.36 V). The stable photocurrent plateau observed in the chopped chronoamperometric curve's light on and off regions confirms sufficient band bending in the TNA material, reducing local charge recombination. Hence, the reduced TNA electrode has greater potential as a HER cathode in the integrated system.

EIS analysis provides information on the resistive layer thickness between the electrode and the electrolyte. Fig. 3c reveals a wider resistive barrier for the anodized TNA electrode, primarily due to surface roughness caused by the lack of annealing. In contrast, the reduced TNA electrode showed a much narrower resistive barrier, directly related to improved HER rates. EIS analysis of reduced TNA electrodes under dark conditions exhibited a greater resistive barrier than under the light conditions (Fig. 3d), confirming light-induced formation of a higher conductive layer, resulting in further enhanced HER performance. In another study, Jeong et al. reported that the reduced TNA's lower resistive layer was due to decreased charge transfer resistance at $Ti^{3+}$ and oxygen vacancy sites compared to only annealed electrodes [23].

### 3.3. Fertilizer-drawn forward osmosis (FDFO) performance

The FDFO system employed a flat sheet commercial thin-film composite (TFC) FO membrane and two solution streams: DS as SBSS, similar to the PEC system's catholyte, and FS as brackish water. To ensure sufficient osmotic energy for FO operation, DS (0.16 M $(NH_4)_2SO_4$ with 4.1 bar osmotic pressure) was maintained at a concentration three times higher than FS (3 g·L$^{-1}$ NaCl with 1.26 bar osmotic pressure). FO runs were performed in FO mode, with the AL facing the feed side and the SL facing the draw side. Membrane characteristics are provided in supporting information (Figs. S3-S5).

Surface wettability and membrane's ability to balance fluid influx and outflux are crucial features governing FO performance. Evaluating surface energy offers insight into surface exposure and bulk interactions. Thus, the surface energy was determined using the contact angles of the membrane with various solvents, applying the Owens, Wendt, Rabel, and Kaelble (OWRK) model. The contact angles of AL in the fresh

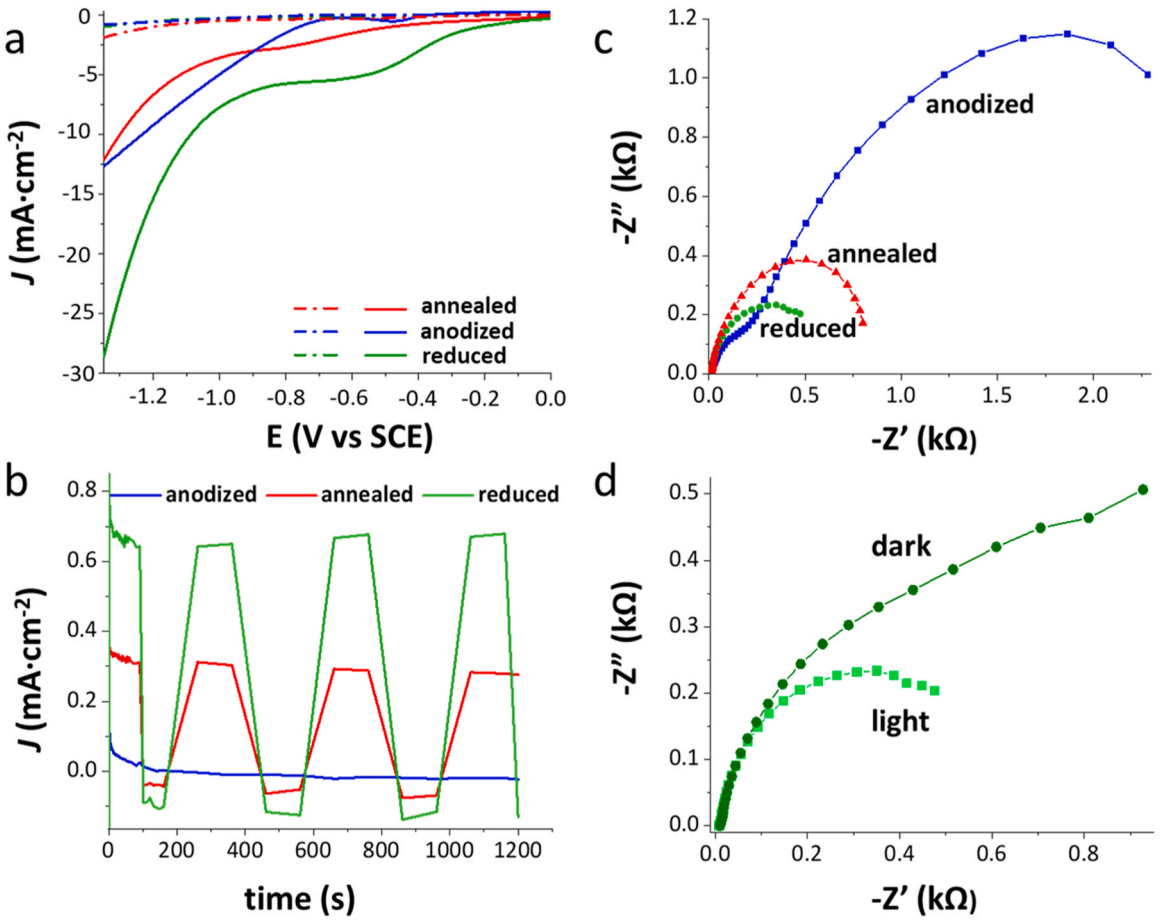


**Fig. 3.** Photoelectrochemical characterization of fabricated TNA electrodes. (a) CV curves; the solid line represents the 'light on' experiment, and the dashed line refers to the 'light off' condition for the same experiment. (b) Chopped chronoamperometry. (c) EIS measurement taken in light for anodized, annealed, and reduced TNA electrodes. (d) Comparison of EIS responses of a reduced TNA electrode under light and dark conditions in 0.1 M $(NH_4)_2SO_4$ electrolyte within the frequency range of 100 kHz to 0.01 Hz.

membrane were 60 ± 1.2°, 36 ± 1.6°, and 0° in DIW, ethylene glycol, and formamide, respectively, yielding a surface energy of 48.6 mJ·m$^{-2}$. A similar surface energy was observed in another study using a home-made poly(ethylene glycol) phenyl ether acrylate (PPEA) active layer. The surface energy (42.95 mJ·m$^{-2}$) of pure PPEA decreased to 40.37 mJ·m$^{-2}$ when 25 % PPEA was replaced with methacrylic acid (MAA) in a 75:25 (w/w %) ratio of PPEA to MAA copolymer system [30]. Moreover, this positive surface energy value could reduce foulant-membrane interaction and ion concentration polarization (ICP), preventing water flux decrease from FS to DS [31].

The FDFO system performance was assessed at various operating flow rates of 0.5, 0.8, and 1.0 LPM (Fig. S6), with FS and DS maintained at the same flow rate. Water flux and % water recovery increased with rising flow rates. At 0.5 LPM, the water flux reached 27.0 LMH with 2.45 % water recovery. Raising the flow rate to 0.8 LPM boosted the recovery to 2.5% and flux to 28.3 LMH, while at 1.0 LPM, recovery and flux increased to 2.88 % and 31.8 LMH, respectively. The pumping flow rate indirectly and inversely represents inflow residence time within the FO chamber; increasing the pumping flow rate reduces interaction time with the FO membrane. Besides water flux and recovery, the flow rate substantially impacts DS solution quality concerning salt rejection and reverse solute flux. At 1.0 LPM, a flux of 31.8 LMH and 2.86 % water recovery were observed, with an impressive 99.3 % salt rejection. Salt rejection at 1.0 LPM was comparable to those at 0.5 LPM (99.4 %) and 0.8 LPM (99.3 %). Consequently, subsequent integrated PEC-FDFO system experiments were conducted at a 1.0 LPM working flow rate.

### 3.4. Integrated PEC-FDFO system for fertigation

The previously described individual FDFO and PEC systems were combined in a tandem configuration. During operation, SBSS first entered the PEC system, underwent hydrogen evolution, and then the outlet stream of the PEC entered the DS side of the FO system. The integration altered the DS flow path in the FO system and streamlined it with an additional peristaltic pump, as shown in Fig. 1.

The initial evaluation of the integrated system was performed using a single component $(NH_4)_2SO_4$ DS. The FDFO desalination performance, as a function of DS concentration, was monitored for 2 h at 1.0 LPM with a constant 3 g·L$^{-1}$ NaCl FS concentration. Test runs were conducted with four different $(NH_4)_2SO_4$ DS concentrations (0.16, 0.20, 0.24, and 0.36 M). Results showed water flux and % water recovery increased with rising DS concentration from 0.16 M to 0.24 M $(NH_4)_2SO_4$, while the water flux for 0.36 M $(NH_4)_2SO_4$ was lower than expected at 23 LMH water flux (Fig. S7). In contrast, 0.24 M $(NH_4)_2SO_4$ generated a higher flux of 32 LMH. Although the osmotic gradient, visualized by the DS and FS concertation difference, is the primary driving force for increased flux, concentration polarization (CP) might negatively impact water flux. Within the asymmetric membrane's porous layer (Fig. S3), a virtual boundary layer shields the membrane from turbulence and shear force. This internal concentration polarization (ICP) reduces the effective osmotic driving force between FS and DS, even though DS exhibits an osmotic pressure of 9.63 bar and FS 1.26 bar, creating an osmotic gradient of 8.37 bar. Thus, it is reasonable to observe lower water flux at 0.36 M $(NH_4)_2SO_4$.

Proceeding to the practical purpose of integrating PEC and FDFO systems, the electrolyte and DS solution used were prepared as single and binary mixtures of $(NH_4)_2SO_4$ and $(NH_4)_2SO_3$ SBSS with a total concentration of 0.24 M. Binary solutions were prepared with three different salt ratios (i.e., 3:2, 1:1, 2:3) of $(NH_4)_2SO_4$:$(NH_4)_2SO_3$. Similar to previous FDFO runs, FO performance was evaluated in terms of water flux and recovery, while PEC performance was assessed through CV (Fig. 4). One CV test was carried out 10 min after the test began to ensure system stability, and another was performed at the end of the 2 h operation of the integrated PEC-FO system. The reduced TNA electrode, as a Pt-free HER catalyst, performed well with a cathodic current oscillating around − 20 mA·cm$^{-2}$ at an electrode potential of − 1.0 V (vs. SCE). Additionally, the cathodic current change at − 1.0 V (vs. SCE) after 2 h was less than 4 % of the initial value, confirming the suitability of the sulfur-based binary electrolyte for hydrogen generation.

Observed trends in current density were based on the sulfite to sulfate ratio in the starting electrolyte. At potentials above − 1.0 V (vs. SCE), the current density increased with rising sulfite content until the sulfite to sulfate ratio reached 1:1, with the current density order being (1:0) < (3:2) < (1:1). The lowest current density was observed in the 2:3 ($(NH_4)_2SO_4$:$(NH_4)_2SO_3$) system (Fig. S8). After 2 h of PEC-FDFO operation, the cathodic current initially dropped but remained high enough (minimum −10 mA·cm$^{-2}$) to ensure the integrated process's operability even at high dilution levels. Conversely, the change in current density after 2 h of PEC-FDFO operation at − 1.0 V (vs. SCE) was insignificant for all single and binary combinations. Regardless of the measured potential, the ammonium sulfite alone system maintained higher current density, while the ammonium sulfate alone system maintained a constant current density during the 2 h PEC-FDFO run. This is due to hydrogen evolution occurring in the complementary reduction process as a result of potential sulfite-to-sulfate oxidation. Water flux increased with higher ammonium sulfate concentration in ammonium sulfite: ammonium sulfate binary solutions, ranging from 13 LMH for 0.24 M $(NH_4)_2SO_3$ solution to 45 LMH with 0.24 M $(NH_4)_2SO_4$. The % water recovery in this scenario, where the operation was conducted for only 2 h, followed a similar pattern to that of water flux (Fig. 4a).

The system increased the total SBSS salt concentration of the DS to 1 M in the integrated process. Water flux and recovery of the integrated process were in a similar range (Fig. 5a) and comparable to a single FDFO system previously studied by our research team [18]. Despite continuous dilution, the PEC maintained a constant potential of − 1.0 V (vs. SCE) until the integrated system completed collecting a large amount of hydrogen gas. In all cases except for 0.6:0.4 or 0.4:0.6, hydrogen evolution measured at − 1.0 V for 5 h (18,000 s) (Fig. 5b) provided a stable current and gradually increased the cathodic current until equilibrium was reached. Interestingly, when the sulfite: sulfate ratio was closer to 1:1 (either 0.6:0.4 or 0.4:0.6), the gradual change in the respective chronoamperometric current over time was minimal compared to other solution compositions. Among binary mixtures, the most stable cathodic current density of 0.15 A·cm$^{-2}$ was observed in the solution where the concentration of $(NH_4)_2SO_3$ (0.8 M) was higher than $(NH_4)_2SO_4$ (0.2 M). The hydrogen evolution performance in the integrated system is comparable to TNA under sodium sulfite ($Na_2SO_3$) and sodium sulfide ($NaS_2$) binary electrolyte with a total salt concentration of 1 M under light irradiation (100 W·m$^{-2}$, AM 1.5 G) [22]. During the integrated PEC-FDFO operation, the ammonium sulfate electrolyte system was slightly acidic (pH 5–6), while the binary solution and ammonium sulfite were near the neutral pH range (pH 7–8). In these scenarios, hydrogen evolution is likely driven by an initial water dissociation step (R4), generating H−adsorbate ($H_{ads}$) at the surface adsorption sites on the electrode, which is regarded as '*E*', followed by the recombination of $H_{ads}$ to produce hydrogen (R5-R6).

$$E + H_2O + e^- \leftrightarrow EH_{ads} + OH^- \quad (R4)$$

$$EH_{ads} + H_2O + e^- \leftrightarrow E + H_2 + OH^- \quad (R5)$$

$$2EH_{ads} \leftrightarrow 2E + H_2 \quad (R6)$$

Long tubular titania nanoarrays in the cathode electrode enhance the solid-solution interface, promoting radial transfer of minority charge carriers into the solution. This vector charge transfer results in an elevated reaction rate when light absorption by the electrode is optimal [22].

Detailed evaluation of the DS and FS solution compositions after 5 h of PEC-FDFO operation showed the highest salt rejection (98.56 % for $Na^+$ and 98.33 % for $Cl^-$) and lowest reverse solute flux (RSF) (3.5 gMH for $SO_4^{2-}$, 5.25 gMH for $SO_3^{2-}$, 3.10 gMH for $NH_4^+$) for the 0.8:0.2 ratio of $(NH_4)_2SO_3$:$(NH_4)_2SO_4$ among binary mixtures (Fig. 5c). However, the RSF was higher at 0.8:0.2 $(NH_4)_2SO_3$:$(NH_4)_2SO_4$ compared to other binary solution combinations (Fig. 5d). As pH in sulfurous electrolytes increases, specific RSF (SRSF) rises, and the water flux decreases. Higher ammonium sulfite content in the above case led to pH 7.65 compared to pH 5.31 for 1 M ammonium sulfate. The RSF was 6.8 gMH for $SO_3^{2-}$ and 4.2 gMH for $NH_4^+$, respectively. Johnson et al. justified such behavior, stating that if a large osmotic pressure gradient exists between FS and DS across the FO membrane, the DS dilutes further until the osmotic

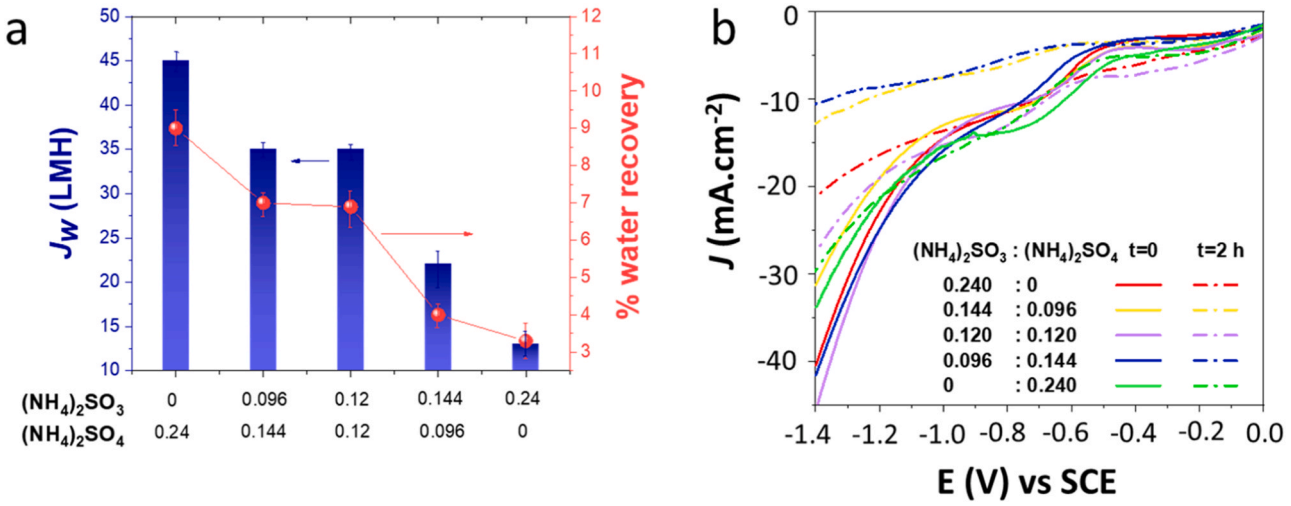


**Fig. 4.** Performance of an integrated PEC-FDFO system at FS concentration of 3 g·L$^{-1}$ NaCl, flowrate of 1 LPM, and run time of 2 h. (a) Water flux and % water recovery vs. various ratios of DS component concentrations at a total DS concentration of 1 M. (b) Corresponding CV curves representing current density (*J*) vs. potential (*E* vs. SCE) measured in the PEC part of the integrated system operation.

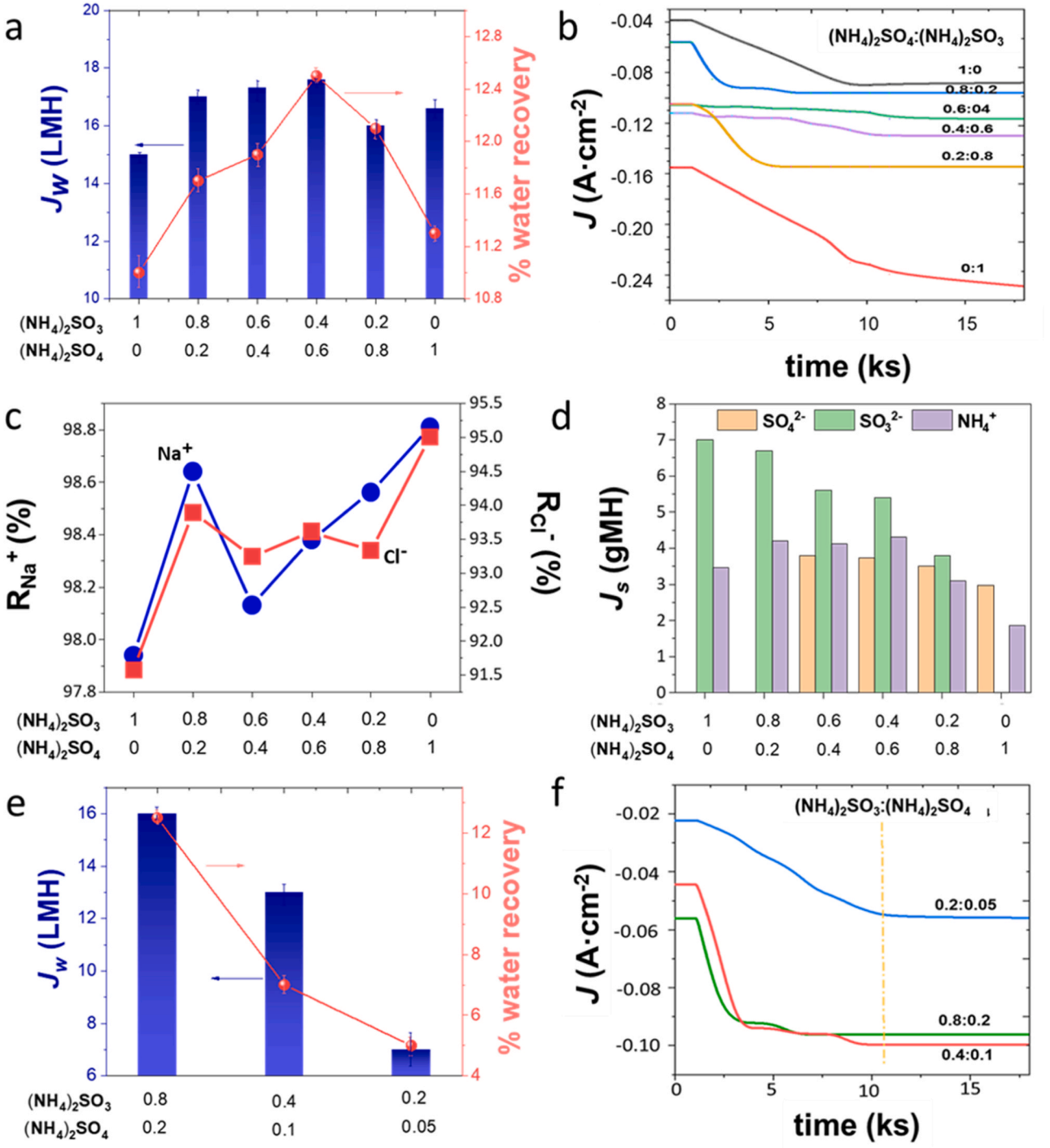


**Fig. 5.** Performance of integrated PEC-FDFO system at an FS concentration of 5 g·L$^{-1}$ NaCl, a total DS concentration of 1 M with different DS component concentration ratios, and a flow rate of 1 LPM. (a) Water flux ($J_w$) and % water recovery vs. various ratios of DS component concentrations. (b) Corresponding chronoamperometric curve measured at − 1.0 V (vs. SCE) vs. current density ($J$). (c) Individual $Na^+$ and $Cl^-$ salt rejection (R %) vs. various ratios of DS component concentrations. (d) Reverse solute flux ($J_s$) vs. different ratios of DS component concentrations. (e) Water flux ($J_w$) and % water recovery vs. various ratios of DS component concentrations at a constant 4:1 molar ratio of $(NH_4)_2SO_3$:$(NH_4)_2SO_4$. (f) Corresponding current density ($J$) vs. time measured in the PEC system at − 1.0 V (vs. SCE).

pressure difference reaches equilibrium [32]. Having minimal salt (< 2 mS·cm$^{-1}$) in the diluted DS is essential for direct use in fertigation, but it should also consider trade-offs between water flux and dilution rate. Theoretically, increased DS salinity should improve water flux and recovery rate, but experimental results show that water flux from FS to DS decreases over time at high DS due to dilutive internal concertation polarization (DICP) and RSF. DICP becomes dominant when more dilution occurs within the SL of the FO membrane facing the DS side, reducing DS osmotic pressure and lowering the effective osmotic pressure gradient across the FO membrane [33]. Conversely, RSF becomes significant at high DS concentrations as it induces DS solute diffusion across the membrane toward the FS side [34]. Therefore, according to water flux and water quality data along with chronoamperometric data, the 0.8:0.2 ratio of $(NH_4)_2SO_3$:$(NH_4)_2SO_4$ offers the most appropriate

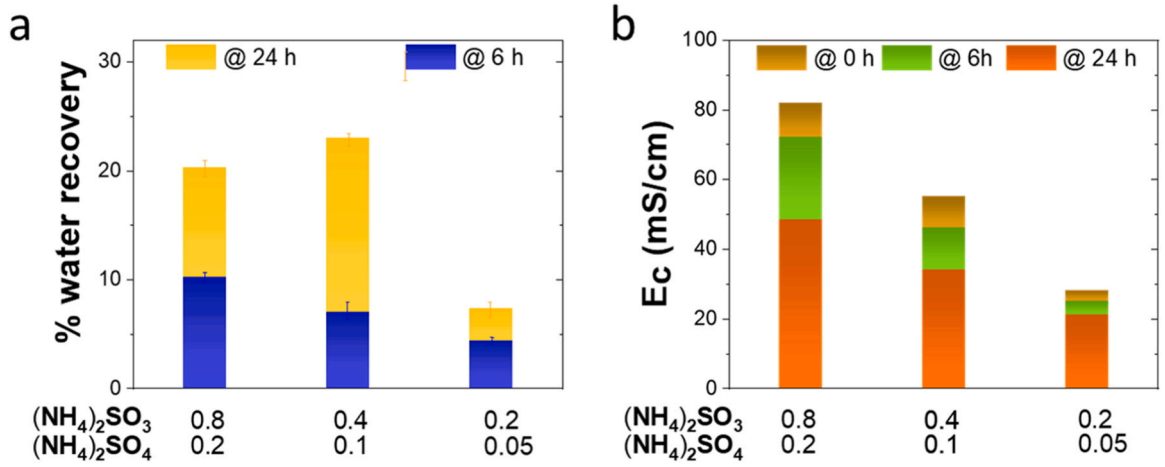


**Fig. 6.** Evaluation of FDFO system in an integrated PEC-FDFO system after 6 and 24 h of operation. (a) Variation of % water recovery vs. various ratios of DS component concentrations. (b) Comparison of conductivity drop vs. various ratios of DS component concentrations.


**Fig. 7.** Evaluation of basil plant growth with diluted DS compared to the control over time (in days). Plants labeled 's' were fed with the diluted DS.

solute ratio with optimal water desalination and energy harvesting properties.

Based on salinity values, the highest % dilution was observed for DS using 0.4 M $(NH_4)_2SO_3$ and 0.6 M $(NH_4)_2SO_4$. However, the PEC system shows higher cathodic current with increasing sulfite content. As sulfite converts to sulfate in the coupling anodic process during HER at the working electrode, the sulfite content facilitates and affects HER, as shown in Fig. 5b. Continuous dilution of the integrated system gradually changes the DS salt concentration. Hence, considering a sequential 50 % dilution level, system operability was assessed with two different salt concentrations (0.5 M and 0.25 M) while maintaining the same 4:1 ratio between ammonium sulfite and ammonium sulfate.

Although a fixed 4:1 ratio of $(NH_4)_2SO_3$:$(NH_4)_2SO_4$ was applied to the FO, the water flux and % water recovery decreased proportionally as the total DS salt concentration decreased (Fig. 5e). The chronoamperometric performance trend at − 1.0 V was similar to that of water flux. In all three systems, cathodic current densities initially stabilized for a short time and then continued to increase until reaching equilibrium (Fig. 5f), due to the simultaneous electrochemical involvement of ammonium sulfite. In this case, the 0.4:0.1 ratio had the highest cathodic current density (0.1 $A{\cdot}cm^{-2}$) at equilibrium compared to other cases. However, DS salinity decreased more rapidly for the 1 M (0.8:0.2) case than for others, as the highest degree of dilution (% water recovery) is expected at a high total DS concentration. Evidently, long-term FDFO operation with a high concentration of DS shows improved water recovery compared to starting with a low concentration of DS when the FS remains constant. Consequently, an FDFO system operating for 6 h in integrated mode was extended an additional 18 h in the standalone FDFO mode for a total operating time of 24 h.

In long-term FDFO operation, water flux decreased from 6 to 24 h as expected, yet % water recovery in the DS side increased significantly (more than doubled) with the % dilution, as shown in Fig. 6a. Also, Fig. 6b demonstrates that the solution resulting from the 24-h operation of the FO with the 0.8:0.2 ratio has a conductivity much closer to the initial conductivity of the 0.4:0.1 ratio solutions. Dilutions greater than 40% from the initial concentration show promise and warrant further investigation.

Besides process integration and favorable performances, the stability of the FO membrane and the reduced TNA electrode through multiple integrated cycles is crucial. To assess the morphology of AL in the FO membrane, SEM analysis was conducted after 10 cycles of PEC-FDFO operation in 0.2 M $(NH_4)_2SO_4$ and 0.8 M $(NH_4)_2SO_3$ DS. The surface features of AL at the 5 μm scale revealed no appreciable scale formation or rupture (Fig. S9a). Additionally, the surface energy test performed on the dried membrane yielded a surface energy of 47.7 $mJ{\cdot}m^{-2}$, which was a negligible reduction compared to the fresh membrane's surface energy (48.6 $mJ{\cdot}cm^{-2}$). Likewise, the reduced TNA electrode visualized by SEM exhibited no significant changes in the tubular structure or surface agglomeration, confirming the recyclability of the FO membrane and the reduced TNA electrode in the PEC-FDFO system (Fig. S9b).

### 3.5. Evaluation of fertigation performance by basil plant growth

Plant growth was evaluated by comparing two basil plants grown side by side, one nourished with municipal water and the other with a diluted solution from a DS reservoir after operating the integrated system. To better understand shoot growth, leaf number and stem height were tracked over time (Fig. S10). The plant fed with DS exhibited remarkable growth in both leaf number and stem height from day 9, outperforming the municipal water-fed counterpart. DS-fed plants consistently had more than double the leaf count of those fed with municipal water. Moreover, leaves matured over time and grew larger in size. The stem height of DS-fed plants increased linearly until day 45, after which exponential growth was observed, potentially due to the rapid development of stem-derived branches (stem height in Fig. S10b includes cumulative height of stem and branches). These findings emphasize the added benefits of using sulfur-containing electrolytes in fertigation over municipal water in terms of leaf density. The significant growth observed in Fig. 7 and S11 may be attributed to sulfur presence in DS. While nitrogen, phosphorous, and potassium (NPK) are primary nutrients for plants, sulfur is essential for chlorophyll production and nitrogen metabolism [35]. This study visually demonstrates the critical role of sulfur in promoting plant growth.

## 4. Conclusion

Addressing the need for a self-sustainable water, energy, and food nexus, this study effectively employed FGD-products-derived SBSS to generate significant hydrogen photocurrents at a reduced TNA cathode in a light-induced electrochemical system while concurrently oxidizing SBSS at a complementary anode. The PEC system effluent is channeled to the FO system as DS, where brackish water (5 $g{\cdot}L^{-1}$) serves as FS, enabling water flux toward the DS side through an osmotic pressure gradient and resulting in substantial DS dilution for fertigation. The optimal DS, composed of 0.8 M $(NH_4)_2SO_3$ and 0.2 M $(NH_4)_2SO_4$, exhibited a stable chronoamperometric current of 0.15 $A{\cdot}cm^{-2}$ at − 1.0 V (vs. SCE), with dilutions of 20 % and 43 % after 6 h (integrated) and 24 h (individual) system operation, respectively. The diluted DS's efficacy for plant growth was verified by monitoring basil plant growth compared to a control group fed with plain water. Increased leaf density and stem height in the test plants highlight sulfur's contribution to plant growth.

The PEC-FDFO system offers several advantages over standalone operation. A key benefit is the hydrogen-rich DS produced by the PEC system. Recent research has focused on hydrogen-rich water's role in plant growth and its anti-oxidant properties [36,37], with the observed substantial growth in leaf density and stem (and branches) height attributable to hydrogen-rich water and nutrients like sulfur. The combined system also enables the use of high sulfite concentrations in FDFO system. Moreover, the adhesion, stability, and durability of reduced TNA film electrodes are exceptional, making them suitable for commercialization. Replacing the Pt counter electrode with cost-effective alternatives such as activated carbon (AC) or graphite would enable small test units of this integrated system to be deployed in agricultural areas with limited energy resources. This study significantly contributes to the WEF field as the first scientifically proven solution demonstrating the transformation of FGD products from serious air pollutants to address all aspects of the water, energy, and food nexus, with tangible results at each stage.

## CRediT authorship contribution statement

**Sifani Zavahir:** Writing – original draft, Methodology. **Tasneem Elmakki:** Methodology, Visualization. **Mona Gullied:** Writing – original draft, Methodology, Software. **Ho Kyong Shon:** Writing – review & editing. **Hyunwoong Park:** Writing – review & editing. **Konstantinos E. Kakosimos:** Writing – review & editing. **Dong Suk Han:** Conceptualization, Writing – review & editing, Supervision, Funding acquisition.

## Declaration of Competing Interest

The authors declare the following financial interests/personal relationships which may be considered as potential competing interests: Dong Suk Han reports financial support was provided by Qatar National Research Fund.

## Data availability

Data will be made available on request.

## Acknowledgements

This study was made possible by financial support from the Qatar National Research Fund (QNRF) under National Priorities Research Grant (NPRP) grant (NPRP 9-052-2-020). Open Access funding was provided by the Qatar National Library (QNL). SEM images were acquired in the Central Laboratories Unit (CLU) at Qatar University. H.P. is grateful to the National Research Foundation of Korea (2018R1A6A1A03024962, 2019R1A2C2002602, and 2021K1A4A7A0 2102598).

## Appendix A. Supporting information

Supplementary data associated with this article can be found in the online version at doi:10.1016/j.jece.2023.110525.

## References

[1] P. Córdoba, Status of flue gas desulphurisation (FGD) systems from coal-fired power plants: overview of the physic-chemical control processes of wet limestone FGDs, Fuel 144 (2015) 274–286.
[2] K.P. Resnik, J.T. Yeh, H.W. Pennline, Aqua ammonia process for simultaneous removal of $CO_2$, $SO_2$ and $NO_x$, Int. J. Environ. Technol. Manag. 4 (2004) 89–104.
[3] Y. Jia, Q. Zhong, X. Fan, X. Wang, Kinetics of oxidation of total sulfite in the ammonia-based wet flue gas desulfurization process, Chem. Eng. J. 164 (2010) 132–138.
[4] R.K. Srivastava, W. Jozewicz, Flue gas desulfurization: the state of the art, J. Air Waste Manag. Assoc. 51 (2001) 1676–1688.
[5] C.R. McLarnon, J.L. Duncan, Testing of ammonia based $CO_2$ capture with multi-pollutant control technology, Energy Procedia 1 (2009) 1027–1034.
[6] F. Artioli, M. Acuto, J. McArthur, The water-energy-food nexus: an integration agenda and implications for urban governance, Polit. Geogr. 61 (2017) 215–223.
[7] R. Mohtar, R.G. Lawford, J.A. Engel-Cox, Achieving water-energy-food nexus sustainability: a science and data need or a need for integrated public policy? Front. Environ. Sci. 8 (2020) 132.
[8] C. Ramirez, Y. Almulla, F.F. Nerini, Reusing wastewater for agricultural irrigation: a water-energy-food nexus assessment in the north western sahara aquifer system, Environ. Res. Lett. 16 (2021), 044052.
[9] J.O. Botai, C.M. Botai, K.P. Ncongwane, S. Mpandeli, L. Nhamo, M. Masinde, A. M. Adeola, M.G. Mengistu, H. Tazvinga, M.D. Murambadoro, A review of the water–energy–food nexus research in Africa, Sustainability 13 (2021) 1762.
[10] H.E. Megerle, S. Niragira, The challenge of food security and the water-energy-food nexus: Burundi case study, in: in: Hidden Hunger and the Transformation of Food Systems, Karger Publishers, Basel, 2020, pp. 183–192.
[11] A.M. Urbinatti, M. Dalla Fontana, A. Stirling, L.L. Giatti, 'Opening up' the governance of water-energy-food nexus: towards a science-policy-society interface based on hybridity and humility, Sci. Total Environ. 744 (2020), 140945.
[12] M.T. Kashifi, F.S.M. Al-Ismail, S. Chowdhury, H.M. Baaqeel, M. Shafiullah, S. P. Tiwari, S.M. Rahman, Water-energy-food nexus approach to assess crop trading in Saudi Arabia, Sustainability 14 (2022) 3494.
[13] K. Huang, L. Dai, L. Yu, Y. Fan, G. Huang, Y. Xiao, Q. Wu, Planning regional-scale water-energy-food nexus system management under uncertainty: an inexact fractional programming method, J. Contam. Hydrol. 247 (2022), 103985.
[14] G.-F. Sargentis, P. Siamparina, G.-K. Sakki, A. Efstratiadis, M. Chiotinis, D. Koutsoyiannis, Agricultural land or photovoltaic parks? The water–energy–food nexus and land development perspectives in the Thessaly plain, Greece, Sustainability 13 (2021) 8935.
[15] S.S. Veroneau, D.G. Nocera, Continuous electrochemical water splitting from natural water sources via forward osmosis, Proc. Natl. Acad. Sci. USA 118 (2021), e2024855118.
[16] B.E. Logan, L. Shi, R. Rossi, Enabling the use of seawater for hydrogen gas production in water electrolyzers, Joule 5 (2021) 760–762.

[17] R.T. Porter, M. Fairweather, M. Pourkashanian, R.M. Woolley, The range and level of impurities in $CO_2$ streams from different carbon capture sources, Int. J. Greenh. Gas Control 36 (2015) 161–174.
[18] S. Phuntsho, H. Park, D.S. Han, H.K. Shon, Sulfur-containing air pollutants as draw solution for fertilizer drawn forward osmosis desalination process for irrigation use, Desalination 424 (2017) 1–9.
[19] Y. Cai, W. Shen, J. Wei, T.H. Chong, R. Wang, W.B. Krantz, A.G. Fane, X. Hu, Energy-efficient desalination by forward osmosis using responsive ionic liquid draw solutes, Environ. Sci. Water Res. Technol. 1 (2015) 341–347.
[20] S. Zou, H. Yuan, A. Childress, Z. He, Energy consumption by recirculation: a missing parameter when evaluating forward osmosis, Environ. Sci. Technol. 50 (2016) 6827–6829.
[21] Z. Liu, H. Bai, J. Lee, D.D. Sun, A low-energy forward osmosis process to produce drinking water, Energy Environ. Sci. 4 (2011) 2582–2585.
[22] U. Kang, K.J. Park, D.S. Han, Y.-M. Kim, S. Kim, H. Park, Photoelectrochemical hydrogen production using CdS nanoparticles photodeposited onto Li-ion-inserted titania nanotube arrays, Catal. Today 303 (2018) 289–295.
[23] H.W. Jeong, K.J. Park, D.S. Han, H. Park, High efficiency solar chemical conversion using electrochemically disordered titania nanotube arrays transplanted onto transparent conductive oxide electrodes, Appl. Catal. B Environ. 226 (2018) 194–201.
[24] X. Hu, L. Chen, Y. Zhang, Q. Hu, J. Yang, Y. Chen, Large-scale flexible and highly conductive carbon transparent electrodes via roll-to-roll process and its high performance lab-scale indium tin oxide-free polymer solar cells, Chem. Mater. 26 (2014) 6293–6302.
[25] G.S. Gund, D.P. Dubal, S.S. Shinde, C.D. Lokhande, Architectured morphologies of chemically prepared NiO/MWCNTs nanohybrid thin films for high performance supercapacitors, ACS Appl. Mater. Interfaces 6 (2014) 3176–3188.
[26] H.W. Jeong, K.J. Park, Y. Park, D.S. Han, H. Park, Exploring the photoelectrocatalytic behavior of free-standing $TiO_2$ nanotube arrays on transparent conductive oxide electrodes: irradiation direction vs. alignment direction, Catal. Today 335 (2019) 319–325.
[27] C. Xiang, L. Sun, Y. Wang, G. Wang, X. Zhao, S. Zhang, Large-scale, uniform, and superhydrophobic titania nanotubes at the inner surface of 1000 mm long titanium tubes, J. Phys. Chem. C 121 (2017) 15448–15455.
[28] K. Reilly, B. Fang, F. Taghipour, D.P. Wilkinson, Simple and scalable synthesis of vertically aligned anatase nanowires for enhanced photoelectrochemical performance, ACS Appl. Energy Mater. 3 (2020) 8317–8329.
[29] H. Yang, E. Kim, S.H. Kim, M.S. Jeong, H. Shin, Hole trap, charge transfer and photoelectrochemical water oxidation in thickness-controlled $TiO_2$ anatase thin films, Appl. Surf. Sci. 529 (2020), 147020.
[30] P.M. Pardeshi, A.A. Mungray, Photo-polymerization as a new approach to fabricate the active layer of forward osmosis membrane, Sci. Rep. 9 (2019) 1–13.
[31] A. Tiraferri, Y. Kang, E.P. Giannelis, M. Elimelech, Superhydrophilic thin-film composite forward osmosis membranes for organic fouling control: fouling behavior and antifouling mechanisms, Environ. Sci. Technol. 46 (2012) 11135–11144.
[32] D.J. Johnson, W.A. Suwaileh, A.W. Mohammed, N. Hilal, Osmotic's potential: an overview of draw solutes for forward osmosis, Desalination 434 (2018) 100–120.
[33] G.T. Gray, J.R. McCutcheon, M. Elimelech, Internal concentration polarization in forward osmosis: role of membrane orientation, Desalination 197 (2006) 1–8.
[34] S. Zou, M. Qin, Z. He, Tackle reverse solute flux in forward osmosis towards sustainable water recovery: reduction and perspectives, Water Res. 149 (2019) 362–374.
[35] F.-J. Zhao, M. Tausz, L.J. De Kok, Role of sulfur for plant production in agricultural and natural ecosystems, in: in: Sulfur metabolism in phototrophic organisms, Springer, 2008, pp. 417–435.
[36] B. Dong, D. Zhu, Q. Yao, H. Tang, X. Ding, Hydrogen-rich water treatment maintains the quality of rosa sterilis fruit by regulating antioxidant capacity and energy metabolism, LWT 161 (2022), 113361.
[37] W. Cui, P. Fang, K. Zhu, Y. Mao, C. Gao, Y. Xie, J. Wang, W. Shen, Hydrogen-rich water confers plant tolerance to mercury toxicity in alfalfa seedlings, Ecotoxicol. Environ. Saf. 105 (2014) 103–111.